Geophysical Research Letters

RESEARCH LETTER
10.1029/2019GL084040

Key Points:
- We examine a number of fine-scale 2-D permeability models of zero-age upper oceanic crust at hydrothermally active East Pacific Rise 9°50′N
- Our preferred permeability model is constrained by independent permeability estimates from poroelastic response measurements at L-vent
- Numerical model based on fine-scale permeability field predicts hydrothermal pathways that are consistent with seafloor observations

Supporting Information:
- Supporting Information S1
- Movie S1

Correspondence to:
M. Marjanović,
marjanovic@ipgp.fr

Citation:
Marjanović, M., Barreyre, T., Fontaine, F. J., & Escartín, J. (2019). Investigating fine-scale permeability structure and its control on hydrothermal activity along a fast-spreading ridge (the East Pacific Rise, 9°43′–53′N) using seismic velocity, poroelastic response, and numerical modeling. *Geophysical Research Letters*, *46*. https://doi.org/10.1029/2019GL084040

Received 7 JUN 2019
Accepted 3 SEP 2019
Accepted article online 12 SEP 2019

Investigating Fine-Scale Permeability Structure and Its Control on Hydrothermal Activity Along a Fast-Spreading Ridge (the East Pacific Rise, 9°43′–53′N) Using Seismic Velocity, Poroelastic Response, and Numerical Modeling

Milena Marjanović[1], Thibaut Barreyre[2], Fabrice J. Fontaine[1,3], and Javier Escartín[1]

[1]Université de Paris, Institut de Physique du Globe de Paris, CNRS, Paris, France, [2]Department of Earth Science/K. G. Jebsen Centre for Deep Sea Research, University of Bergen, Bergen, Norway, [3]Now at Observatoire du Piton de la Fournaise, Ile de La Réunion, France

Abstract Along with the intracrustal heat source, crustal permeability is considered as the controlling factor for hydrothermal circulation within zero-age oceanic crust. To obtain fine-scale, 2-D models of upper crustal permeability along the East Pacific Rise 9°50′N, known for prolific hydrothermal activity, we use recently derived high-resolution seismic velocity and examine a number of the existing velocity-permeability relationships. To constrain our preferred permeability model, we compare thus derived permeability models with collocated permeability estimates from poroelastic response to tidal loading at L-vent. Furthermore, using the preferred permeability result, we model hydrothermal convection in 2-D and find that the distributions of recharge and discharge zones are in good agreement with seafloor observations, including locations of the vent fields. Our results suggest that seismic velocities can be used as a tool for deriving spatial variation of permeability, which must be considered in modeling of hydrothermal flow.

Plain Language Summary Crustal permeability represents one of the main controlling factors for development and persistence of hydrothermal circulation at mid-ocean ridges. However, this parameter remains poorly constrained. Using recently obtained seismic velocity model and available velocity-permeability relationships, we calculate a number of permeability models for East Pacific Rise 9°50′N region, known for vigorous venting sites, including L-vent. To narrow down a wide range of upper crustal permeabilities and constrain our preferred permeability model, we use measurements obtained from poroelastic response of crustal lithologies to tides at L-vent. Our results suggest that average permeability for the first ~100 m of the upper oceanic crust is $10^{-11.2}$ m^2, whereas 10^{-14} m^2 characterizes the remaining part. We further evaluate our results with numerical models of hydrothermal circulation. The model that uses our preferred permeability field predicts locations of hydrothermal fluid recharge and discharge zones that are consistent with seafloor observations. Our study suggests that a growing number of high-resolution seismic velocity models can be further used to provide first-order estimates of permeability that will help us to advance our understanding behind hydrothermal processes, fluid circulation, and associated exchanges along mid-ocean ridges.

1. Introduction

Circulation of hydrothermal fluids through oceanic crust along mid-ocean ridges (MOR) accounts for ~6% of the total Earth's internal heat loss and plays a major role in lithosphere-ocean thermal, mass, and chemical exchanges (e.g., Elderfield & Schultz, 1996; Sclater et al., 1980; Stein & Stein, 1992). Along fast- to intermediate-spreading centers axial magma lenses (AMLs) with highly molten portions were identified (Canales et al., 2006; Marjanović et al., 2015; Singh et al., 1998; Xu et al., 2014), representing a prerequisite for the formation of high-temperature (i.e., 200–450 °C), high-heat, *smoker-like* hydrothermal activity (Baker, 2009; Marjanović, Fuji, et al., 2017; Wilcock & Fisher, 2004). Together with the thermal properties of the melt-bearing AML, permeability of the axial crust is another controlling factor on the

vigor/dynamics and architecture of hydrothermal convection and heat extraction (e.g., Lowell & Germanovich, 2004). In the past, a significant effort has been put to provide permeability estimates of oceanic crust. However, this task has proven challenging because of the complexity of the involved processes (magmatic, tectonic, and hydrothermal), which operate at different spatial and temporal scales (Lowell & Germanovich, 1994). Some of the available permeability estimates, spanning a wide range of values (10^{-18}–10^{-10} m^2), are derived from in situ borehole measurements or extracted from different parameters obtained from boreholes (Becker, 1989; Fisher, 1998; Becker & Fisher, 2000, 2008; Becker & Davis, 2003; Davis et al., 2010; Fisher et al., 2008; Winslow et al., 2013). It has to be mentioned that all of the boreholes are located off-ridge axis, sampling the crust >1 Myr old at scales that may not be representative of regional permeability of fractured rock (Wilcock & McNabb, 1996). Kilometer-scale hydrothermal flow models at MOR proposed a subrange of average permeabilities for the upper crust, 10^{-15} and 10^{-12} m^2 (Coumou et al., 2008; Driesner, 2010; Hasenclever et al., 2014; Lowell & Germanovich, 2004; Lowell et al., 2013; Theissen-Krah et al., 2011). Finally, a number of recently developed, indirect approaches based on the analysis of the effects of tides on vent temperatures suggested values ranging from 10^{-9} to 10^{-15} m^2 for a narrow zone around vent sites (Barreyre et al., 2014, 2018; Barreyre & Sohn, 2016; Crone et al., 2011). As a result, both the actual permeability and its spatial variation within the upper oceanic crust, dominated by hydrothermal circulation, remain poorly constrained.

One of the biggest challenges in the analysis and interpretation of controlled source seismic data is to link seismic parameters such as seismic velocity to geological properties of rocks in the subsurface. There is a growing number of seismic studies conducted at MORs that provide high-resolution velocity models of oceanic crust in two dimensions (Arnulf et al., 2011, 2012, 2014; Christeson et al., 2012; Marjanović, Fuji, et al., 2017), and lately in three dimensions (Arnoux et al., 2017; Arnulf et al., 2018; Marjanović, Plessix, et al., 2018; Morgan et al., 2016). In addition, it has been suggested that the observed velocity variations in the crust primarily reflect localized variations in porosity, and ultimately in permeability of rocks (e.g., Swift et al., 2008).

To obtain a range of possible permeability models for upper oceanic crust, we use permeability-velocity relationships available in the literature (see section A in Supporting Information, SI). For constraining our preferred permeability model, we compare our permeability estimates obtained from velocity with the permeability estimates from a revisited poroelastic response to tidal loading at L-vent as an independent approach. Finally, we use our preferred permeability model to examine hydrothermal fluid circulation flow along the EPR. We show that variable permeability in the along-axis plane is an important controlling factor on distribution of hydrothermal pathways and should not be neglected in numerical models.

2. Geological Background

Currently, ~500 hydrothermal vent sites have been identified along active plate tectonic boundaries (Beaulieu, et al., 2013, 2015). Among these, the most studied ones are the vents located along the EPR 9°50′N, which are grouped into two clusters: the northern vent cluster that is centered at 9°50′N and the southern at ~9°46′N (Figure 1a). Within the southern cluster, the high-temperature L-vent (9°46′14′′N) shows hydrothermal discharge at temperatures ~355 °C (Barreyre & Sohn, 2016). Both the exit-fluid temperature measurements at this vent site and contemporaneous modeled bottom pressure were analyzed to determine the poroelastic response to tidal loading. These analyses led to estimates of the effective permeability of the underlying crust hosting the hydrothermal circulation (Barreyre et al., 2018): ~10^{-13} m^2 for layer 2A (topmost layer of the oceanic crust represented mostly by basalts) and <10^{-14} m^2 for layer 2B (represented by dikes). It needs to be mentioned that the above results were obtained using averaged values of parameters, such as compressional velocity, porosity, and layer 2A and 2B thicknesses, from earlier studies (e.g., Sohn et al., 2004; Vera et al., 1990) that are not representative of the subsurface at L-vent.

In addition to hydrothermal venting, the EPR 9°50′N is volcanically active, with two documented eruption events in 1991–1992 (Haymon et al., 1991) and 2006 (Tan et al., 2016; Tolstoy et al., 2006). This dynamic magmatic system has been the focus site of a number of active seismic studies (e.g., Detrick et al., 1987; Kent et al., 1993; Mutter et al., 2009; Vera et al., 1990). In the upper oceanic crust, seismic data collected in 2008 revealed a relatively thin layer 2A with an on-axis average thickness ~155 m (for the extent shown in Figure 1a) and somewhat thicker seismic layer 2B with on-axis thickness ~1,345 m (Marjanović, Carbotte, et al., 2018). In addition, an ~1-km-wide AML reflector was observed (Marjanović, Stopin, et al., 2017), sitting ~1.5 km

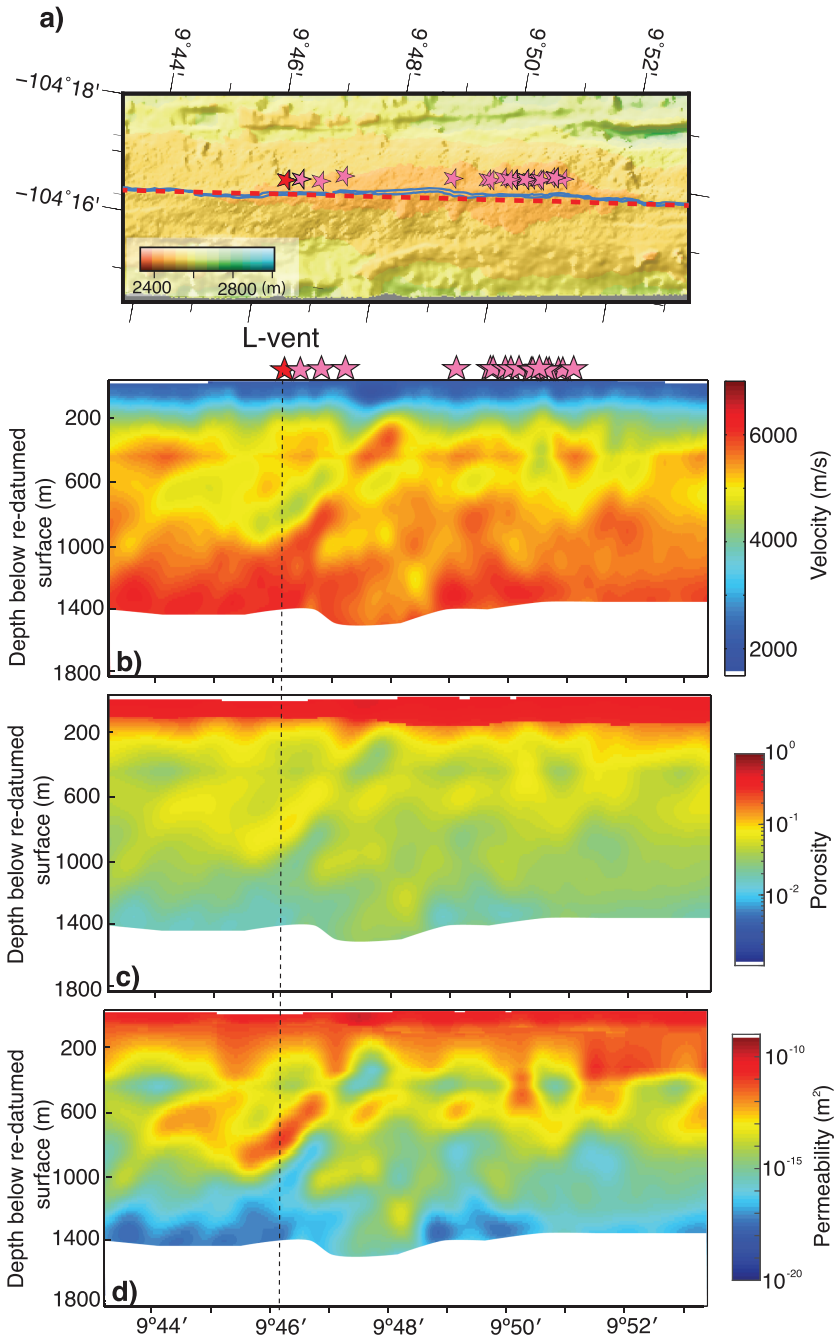

Figure 1. Physical properties of the upper oceanic crust derived from seismic data. (a) Bathymetry map for the extent of the ridge axis examined in this study. The bathymetry data are from White et al. (2006). Red dashed line indicates location of the along-axis 2-D seismic line used to obtain velocity model shown in (b); dark blue line outlines the axial summit through Soule et al. (2009). (b) Two-dimensional compressional velocity (*Vp*) model presented by Marjanović, Fuji, et al. (2017) for the region extending from 9°43′ to 9°53′N. (c) Two-dimensional porosity profile calculated using combined velocity-porosity relationships obtained using effective medium theory for layer 2A and porosity-velocity relationship from Carlson (2011, 2014) for porosities within layer 2B (details are provided in Supporting Information, section A). Note that the color bar is given in logarithmic scale for better visibility. (d) Two-dimensional crustal permeability profile calculated using permeability-velocity relationships (Carlson, 2014; SI, section A). Location of the L-vent is marked in red star and vertical dashed line; locations of the remaining vent sites are indicated in pink stars. Only the areas along the profile with reliable data are shown, and the rest are masked (Marjanović, Fuji, et al., 2017). The redatumed level is at 2,394 m below sea surface.

below seafloor (Carbotte et al., 2013; Marjanović, Carbotte, et al., 2018) and displaying variations in melt content at short spatial scales, <100 m (Marjanović et al., 2015). Furthermore, high-resolution 2-D compressional velocity (*Vp*) structure along axis showed the presence of low-velocity, conduit-like anomalies (<2 km wide) embedded within the upper crust (Marjanović, Fuji, et al., 2017; Figure 1b). Based on their spatial distribution and correlation with the fine-scale tectonic segmentation and the presence of vent sites, these anomalies were associated with upgoing and downgoing pathways of the hydrothermal fluids.

3. Methodology

3.1. Permeability Estimates Derived From Seismic Velocities

We examine a number of permeability-velocity and porosity-permeability relationships (we derive porosity from velocity) available in the literature (Carlson, 2010, 2011, 2014; Slagle & Golberg, 2011; Mavko & Nur, 1997). A detailed description of all of the relationships considered is provided in SI. In all of the examined models, we use the seismic *Vp* model presented by Marjanović, Fuji, et al. (2017), shown in Figure 1b. It is important to mention that we inspect layers 2A and 2B separately, as we expect that the intrinsic structural and textural characteristics of rocks composing these layers (basalts and dikes, respectively) govern the relationships between the parameters in a different manner. The resulting permeability ranges, as well as the average values obtained from all of the considered models, are shown in Tables A1 and A2 in SI. To illustrate the differences in the obtained porosity and permeability functions, we extract a 1-D porosity and permeability profiles at L-vent (Figure A2 in SI) for which we also have permeability estimates from poroelastic approach.

3.2. Permeability Estimates Derived From Poroelastic Response to Ocean Tidal Loading

3.2.1. Phase Lags Estimates

As the basis for our poroelastic modeling, we use the phase lag estimates for exit-fluid high temperature versus tidal pressure by Barreyre and Sohn (2016) at L-vent. At this location phase lag data set consists of two records of about 2.5 years of recording with average and uncertainty values of phase lag of 207° ± 5° at M2 frequency and 188° ± 7° at K1 frequency.

3.2.2. Permeability Estimates

Following the same methodology in conjunction with the multilayer poroelastic model described by Barreyre et al. (2018), we model the predicted phase lag between the tidal bottom pressure and exit-fluid temperature as a function of the coupled layers permeabilities (i.e., k2A and k2B; Figure 2). Here, the baseline inputs of poroelastic parameters, such as seismic velocity and layer thickness, are extracted from seismic studies at L-vent (Marjanović, Fuji, et al., 2017). As an average vertical velocity within layer 2A, we thus obtain ~2.1 km/s and within 2B ~4.96 km/s (Figures 1b, 2a, and 2b and Table 1); the extracted thickness of layers 2A and 2B used in the modeling are 100 and 1,350 m, respectively. As an input value for porosity of layer 2A, we decide to use 44% (Table A2 in SI). This porosity value represents a harmonic mean, obtained from a porosity-velocity relationship derived using a self-consistent approximation within effective medium theory, assuming sphere-like pores (equation A1 and section A in SI). We also conducted tests using average porosity values obtained from other porosity-velocity relationships. However, the resulting variations in permeability are negligible, and hence, we opt for the simplest model. For layer 2B, we adopt porosity of 3.5%, corresponding to the harmonic mean (Table A2 in SI) obtained using the porosity-velocity relationship described by equation A5 (section A and Figure A2a in SI). Other parameters such as densities of both seawater and hydrothermal fluids, bulk modulus, and storage compressibility are from Barreyre et al. (2018). These constraints on crustal and fluid parameters, in concert with our phase lag estimates at both M2 and K1 tidal frequencies, reduce the permissible model solution space to narrow slivers shown as black contours in Figure 2c.

3.3. Setup for 2-D Numerical Modeling

The mathematical framework for our 2-D numerical modeling is based on the approach presented by Fontaine and Wilcock (2007). This approach is a good first-order approximation of hydrothermal flow beneath vapor-like vent sites, such as the ones present at the EPR 9°50′N (e.g., Coumou et al., 2006; Fontaine & Wilcock, 2007). It has to be mentioned that the models with spatially variable permeability fields, such as those derived from seismic velocities, are numerically challenging because of local permeability gradients and/or large permeability ranges. To enable converging solutions, we smooth the permeability field:

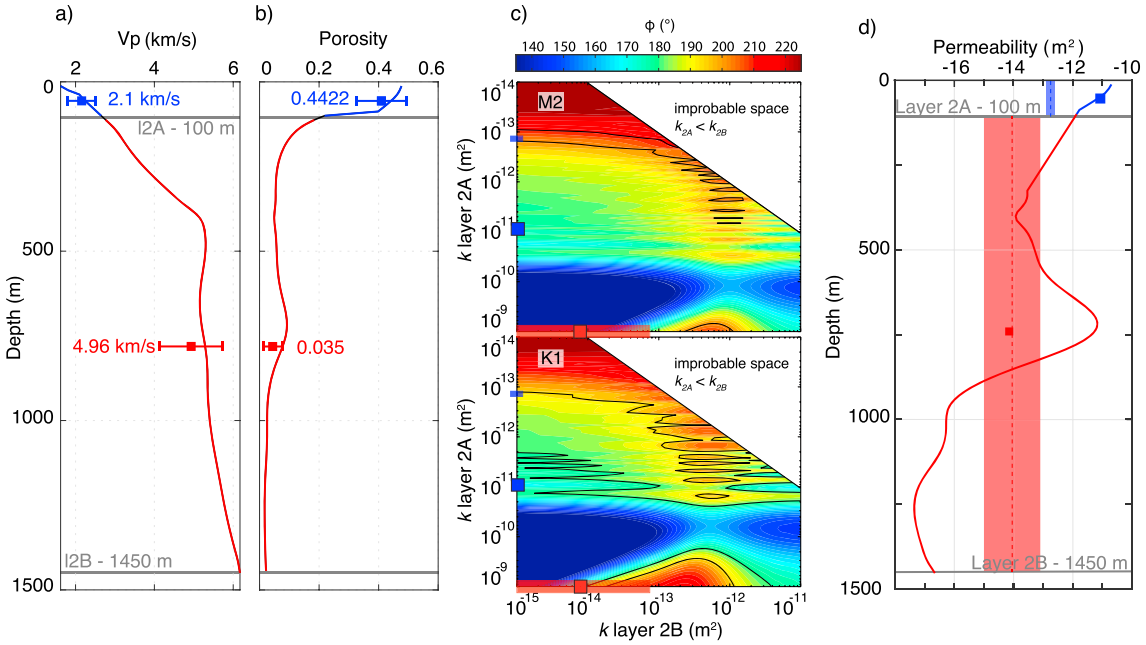

Figure 2. (a) Compressional wave (*Vp*) velocity depth profile beneath the L-vent extracted from 2-D *Vp* model presented by Marjanović, Fuji, et al. (2017) and shown in Figure 1b. Depth-averaged values used in poroelastic modeling are indicated for both layer 2A (blue) and layer 2B (red). (b) Porosity depth profile beneath L-vent estimated from *Vp* extracted at the L-vent site from the 2-D model shown in Figure 1c. Depth-averaged values used in poroelastic modeling are indicated for layer 2A (blue) and layer 2B (red), respectively. (c) Modeled phase lags are plotted as a function of k_{2A} and k_{2B} assuming geometries and properties of layers 2A and 2B as summarized in section 3.2 and following the approach and poroelastic model presented by Barreyre et al. (2018). Contours of observed phase lags at the L-vent are shown in black. Top and bottom panels represent M2 and K1 tidal frequencies, respectively. Note that colored bars on k_{2A} and k_{2B} axes correspond to the combined constrained solution space from M2 and K1 frequencies for the permeability of layer 2A (in blue) and layer 2B (in red). The average values of permeability derived from seismic velocity are shown in blue (for layer 2A) and red (for layer 2B) squares. (d) Permeability depth profile beneath L-vent extracted from 2-D profile shown in Figure 1d. The average values for seismically derived permeability are shown in squares, blue for layer 2A and red for layer 2B. Constrained permeability estimate ranges from panel in (c) are shown as vertical bars for both layer 2A (blue) and 2B (red) with average value indicated in dashed line.

Vp-derived permeability (Figure 1d) is first made dimensionless ($k_{vp\text{-adi}}$) using the maximum of the permeability field, and the smooth permeability (k_s) used in the simulation (Figure 3a) is obtained as follows:

$$ks(x,z) = 2.3\times10-10kvp-\mathrm{adi}(x,z)\times(0.5-(\arctan(10\times(kvp-\mathrm{adi}(x,z)-10-4)))/\pi) \quad (1)$$

This smoothing step reduces locally the permeability gradients, helping to stabilize the simulations without modifying the main characteristics and features of the *Vp*-derived permeability field. The smooth

Table 1
Range and Average (Harmonic Mean) Values of Velocity (Marjanović, Fuji, et al., 2017), Porosity, and Permeability Parameters for Layers 2A and 2B

		Minimum poroelastic response	Maximum poroelastic response	Average poroelastic response	Average derived for the L-vent	Average derived for the 2-D profile	Minimum for the 2-D profile	Maximum for the 2-D profile
Layer 2A	Velocity (km/s)	-	-	-	2.1	2.9	1.7	3.6
	Porosity (%)	-	-	-	44	45	32	53
	Permeability (m^2)	$10^{-12.9}$	$10^{-12.6}$	$10^{-12.75}$	$10^{-11.1}$	$10^{-11.2}$	$10^{-12.7}$	$10^{-10.3}$
Layer 2B	Velocity (km/s)	-	-	-	4.96	5.3	3.6	6.2
	Porosity (%)	-	-	-	3.5	9	1.5	53
	Permeability (m^2)	10^{-15}	$10^{-13.1}$	$10^{-14.05}$	$10^{-14.2}$	10^{-14}	$10^{-17.6}$	$10^{-9.86}$

Note. The precision of the permeability values is to two decimal points as in Carlson (2014).

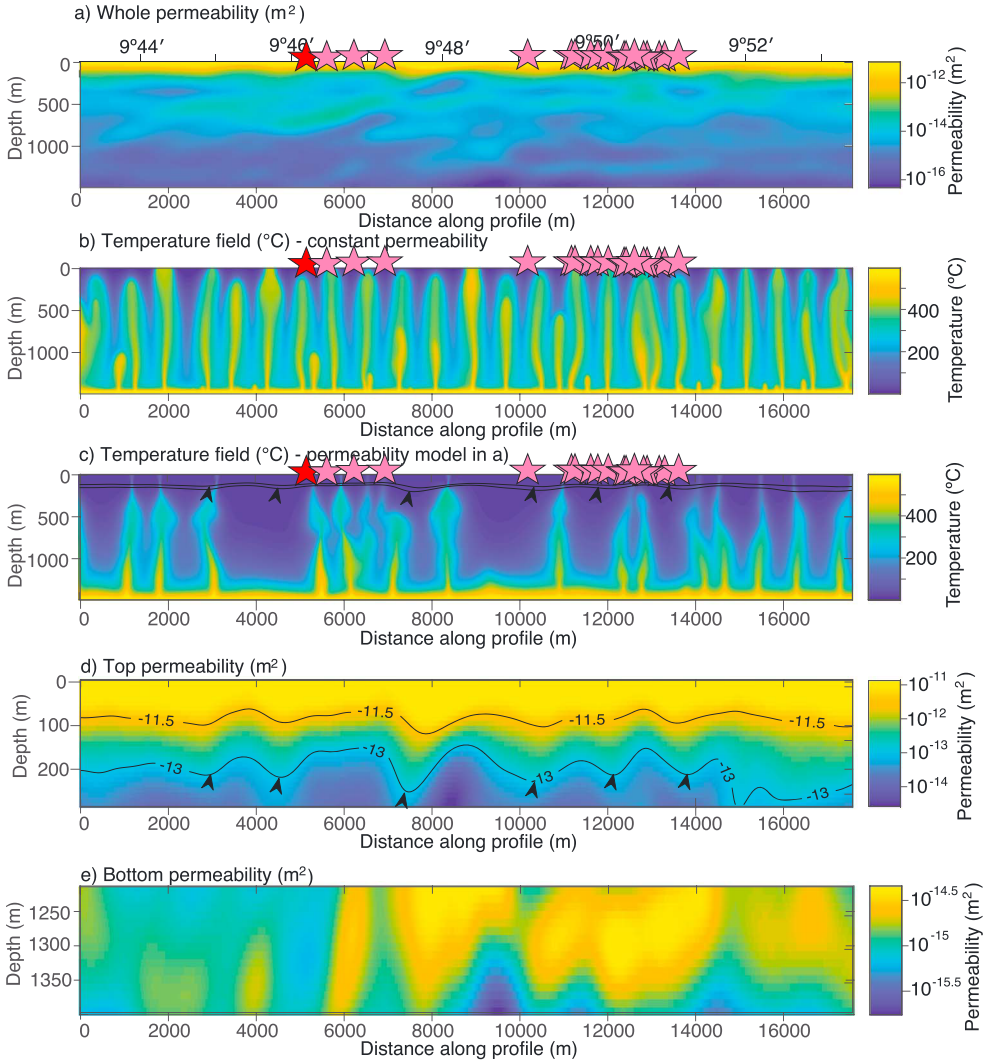

Figure 3. Results of the 2-D numerical simulations (open-top and constant basal temperature, 600 °C) of hydrothermal flow with constant and *Vp*-derived permeability fields. The modeling domain is discretized in square nodes (6.25 × 6.25 m^2). (a) Smooth 2-D permeability field used in the whole model domain. (b) Two-dimensional temperature field for a constant permeability model. (c) Two-dimensional temperature field after 8,200 years for a model with the permeability field of Figure 3a. Red star shows location of L-vent, whereas pink stars show locations of the remaining vents. Red and blue bars on top show the extent of the signal from ephemeral, oxidation-reduction potential (ORP), and broadly dispersing nephelometric turbidity units (NTU), respectively (Baker et al., 2016). See (d) for black lines and arrows. A time lapse of the 2-D temperature field for the period of 8,200 years is shown in SI, section D. (d) Two-dimensional permeability field at the top of the modeling domain (zoom on the last 250 m) highlighting the continuous high-permeability top layer. Black lines are the $10^{-11.5}$ and 10^{-13} m^2 permeability isocontours, and black arrows mark the locations where the high-permeability layer is thicker. In these regions, robust downflows tend to form. (e) Two-dimensional permeability field at the bottom of the modeling domain (zoom on the last 100 m).

permeability distribution controls the heat flux crossing the basal boundary layer and associated Nusselt number (i.e., Nu—the dimensionless conductive heat flux entering the bottom of the simulation box), which is about 10 (Henstock et al., 1993; Phipps Morgan & Chen, 1993), that is, mean basal heat flux ~10 W/m^2. This level of basal heat flux is in reasonable agreement with estimates of the heat flux crossing roots of black smoker systems fossilized in ophiolite (e.g., Troodos and Oman) and at tectonic exposures on the seafloor of the EPR (i.e., 11–44 W/m^2; Gillis, 2008). In addition, we design an experiment with a constant permeability, and to compare simulations with the same thermal performances, we tune this permeability so that its Nusselt number is equal 10. In simulations with *Vp*-derived permeability, the maximum venting

temperature at the top of the box does not exceed 150 °C. This is due to the intense conductive cooling of the rising thermal instabilities as they cross the high-permeability layer topping the domain. In natural systems, it is expected that hydrothermal upflow zones remain thermally insulated from cold seawater in the high-permeability layer 2A (e.g., via precipitation processes; Fontaine & Wilcock, 2007), so that conductive cooling is minimized. Here, we posit that conductive cooling influences only the temperature of upflow zones, and not their distribution.

4. Results and Discussion

4.1. Constraining Permeability Model From Independent Approaches at the L-Vent Site

4.1.1. Layer 2A

Using a number of permeability-velocity relationships presented in section A in SI, we examine nine plausible permeability functions for layer 2A (Figure A2b in SI). The permeability values for layer 2A obtained using permeability-velocity relationship introduced by Carlson (2011) and Mavko and Nur (1997), equations A8 and A10 in SI, respectively, show relatively similar average values. The former indicates that the average permeability is $10^{-11.13}$ m^2, while the latter suggests slightly lower permeability $10^{-12.11}$ m^2 (Table A1 in SI). In contrast, the permeability-velocity relationship introduced by Slagle and Goldberg (2011), equation A11 in SI, results in values that are for 4 orders of magnitude smaller, ~10^{-15} m^2. To provide an independent constraint to our permeability models and narrow the range of plausible layer 2A permeabilities, we examine the results obtained using poroelastic response to tidal loading at L-vent. The permeability values using the poroelastic approach show an average value $10^{-12.75}$ m^2 (Figure 2). This result is relatively close to the estimates obtained using equations A8 and A10 in SI, suggesting that the values obtained by equation A11 in SI are probably not realistic for zero-age basalts. Regarding the former two models, although the results appear similar, they yield to permeability difference of about an order of magnitude higher to those derived from poroelastic approach. The observed difference may be due to (i) high spatial heterogeneity of layer 2A (note the small permeability range obtained from poroelastic approach; Table 1), (ii) the assumptions present in velocity (Marjanović, Fuji, et al., 2017) and poroelastic (Barreyre et al., 2018) modeling, and (iii) different sensitivity of the methodologies (see section B in SI). To keep the model consistent with the assumption we considered for our preferred layer 2A porosity model (section 3.2), we use the results employing Carlson's relationship (A8) as our preferred permeability model (Figure 1d and Table 1).

4.1.2. Layer 2B

For the portion of the upper crust composed predominantly by dikes, we obtain three plausible permeability functions (Figure A2b in SI) with average permeability values ranging between $10^{-16.52}$ and $10^{-14.15}$ m^2 (Table A1 in SI). As in the case of layer 2A, to narrow down this broad range of permeabilities within layer 2B, we compare the results to the permeability estimates obtained from poroelastic response (Figure 2 and Table 1). The latter approach suggests permeability values beneath L-vent ranging between 10^{-15}–$10^{-13.1}$ m^2, with an average value $10^{-14.05}$ m^2. The layer 2B permeabilities derived from seismic velocity using the relationship presented by Carlson (2011), equation A9 in SI, shows a comparable mean value (harmonic mean), $10^{-14.15}$ m^2. Furthermore, this value is consistent with prior estimates of the permeability of smoker-like hydrothermal systems based on heat flux arguments stating that the extraction of hundreds of megawatts requires permeabilities around 10^{-14} m^2 (e.g., Barreyre et al., 2018; Coumou et al., 2006, 2008; Fontaine & Wilcock, 2007). Thus, for layer 2B, we base our preferred permeability model on equation A9 in SI derived by Carlson (2011), which we show in Figure 1d.

4.2. Variation of Upper Crustal Permeability Along the EPR Axis

Our preferred permeability model for the portion of EPR extending between 9°43′ and 9°53′N shows a wide range of upper crustal permeabilities (Figure 2d and Table A1 in SI), which is in good agreement with the permeability estimates provided by convection models (Coumou et al., 2008; Driesner, 2010; Fontaine & Wilcock, 2007; Lowell et al., 2013; Lowell & Germanovich, 2004). The topmost part of the crust shows high permeabilities, ranging from $10^{-12.67}$ to $10^{-10.31}$ m^2. In contrast, the lowest permeabilities are observed within the lower portions of the dike section, with the minimum permeability value of $10^{-17.6}$ m^2. This low-permeability zone could correspond to the impermeable, solid layer that decouples AML from the hydrothermal layer, which is in seismic velocity models seen as higher-velocity zone atop of AML (Singh et al., 1999). The presence of the transition zone was also reported in ophiolites (Gillis, 2002; Gillis &

Roberts, 1999; MacLeod & Yaouancq, 2000; Nicolas & Boudier, 2011; Pedersen, 1986), marked by an abrupt decrease in hydrothermal alteration (Nehlig, 1994).

The most prominent high-permeability anomaly within layer 2B is present beneath the southern vent cluster (Figure 1d), the southernmost of which is L-vent. Based on the observations in velocity model, Marjanović, Fuji, et al. (2017) associated the observed of low-velocity anomaly (here seen as high permeability) with the presence of upgoing pathway of the hydrothermal circulation, connecting with the four vent sites mapped in the seafloor. Another zone of high permeabilities within layer 2B is located beneath the northern vent cluster, which extends between 9°49′ and 9°51′N, and where the average permeability reaches ~10^{-12} m^2. Within this same zone low permeabilities were proposed from the analysis of poroelastically triggered microearthquakes (Crone et al., 2011). For this ~4-km-long stretch of the ridge axis, the above approach suggested variation in permeability from $10^{-13.4}$ to $10^{-9.4}$ m^2 (average 10^{-12} m^2), with the highest values coinciding with the regions of downgoing and upgoing hydrothermal pathways as inferred from microearthquake distribution in 2003–2004 (Tolstoy et al., 2008; Waldhauser & Tolstoy, 2011). Although we observe a similar pattern of permeability highs and lows, our study suggests permeabilities that are 1–2 orders of magnitude lower. As noted by Barreyre et al. (2018), the high-permeability values derived from poroelastically triggered microearthquakes are not consistent with hydrothermal flow observations, as they would result in unrealistically high heat flow around the vents and in temperatures of fluid discharge significantly lower than those observed.

4.3. Insight From 2-D Numerical Models of Hydrothermal Circulation

In Figure 3, we compare solutions of two 2-D numerical simulations: Model in Figure 3b has a constant permeability field, and model in Figure 3c incorporates the smooth version of the *Vp*-derived permeability field (Figure 3a). The converged thermal field of the constant permeability experiment is characterized by a series of symmetrical convection cells of even size (~400 m wide, 1,500 m high), producing regularly spaced discharge and recharge zones along the top of the model box, which does not match seafloor observations. This result depicts typical solution for cellular hydrothermal convection with constant permeability; the size of the convection cells is controlled by the assumed constant permeability value (e.g., Fontaine & Wilcock, 2007). In contrast, the thermal field of the simulation with the *Vp*-derived permeability is spatially complex and largely controlled by discrete permeability features, and particularly at the top and bottom (Figures 3d and 3e). Thin thermal instabilities tend to arise from prominent high-permeability regions at the model's base and rise in the system to produce vent sites (e.g., along the model shown in Figures 3c and 3d at 6,300 and 8,500 m and along an elongated regions between 10,500 and 14,400 m). The *Vp*-derived permeability field displays a continuous high-permeability layer at its top (Figures 3c and 3d). The thickness of this layer is not uniform along the profile with vertical fluctuations <50 m. Locally, thicker regions in this layer tend to stabilize robust downflows. The final temperature structure in the model is controlled by the competition between these hot, rising fronts and cold, sinking fronts. For instance, the model predicts formation of steady 2–3-km-long, downflow areas centered at 5,000 and 10,000 m. These downflow zones form in regions where the permeability is relatively low at the base of the domain (the smallest model permeability is at 10,000 m). Consequently, thermal instabilities are not produced in the bottom boundary layer and the cold sinking fronts produced at the top of the system propagate down to the bottom of the system.

In general, our numerical modeling results are consistent with the geologic observations between 9°43′N and 9°53′N. The two clusters of vents observed in the seafloor are underlain by high-permeability regions from which well-developed and robust upflows arise at the base of the crust (Figure 3a). Our model presented in Figure 3c seems to better reproduce vent sites around L-vent than sites more to the north. However, it is important to emphasize that Figure 3c represents only a snapshot in time of the temperature field at the end of the simulation, when the circulation is stabilized in terms of heat extraction (i.e., when Nu reaches a plateau). The distribution of vent sites evolves through time, and during the transient phase, more upflows are observed in the northern part of the profile (see section C in SI). The current vent distribution in the northern part may represent such a transient phase, while the cluster around L-vent results from a more mature/evolved circulation. In addition, some of the upflows in our model are observed beneath regions that are identified as the regions of hydrothermal discharge that are not represented by vent chimneys on the seafloor and that are mapped in 2011 from continuous tows of receptors sensitive to hydrothermal tracers (Baker et al., 2016). The areas devoid of upflows (e.g., the larger ones in the model at 5,000 and 10,000 m

along the profile) may represent preferential zones of inflows of seawater at the seafloor through shallow high-permeability regions and low permeability above the AML, so that hot thermal instabilities cannot arise. Finally, several upflow fronts are observed devoid of mapped discharge zones. They may represent permeability zones that are not connected to the present-day flow (e.g., abandoned, old upflow zones). In addition, they could reflect 3-D structures that are not taken into account in the numerical modeling nor the permeability/*Vp* estimates (see section B in SI).

5. Conclusions

We present a first-order estimate of permeability field in 2-D obtained from high-resolution seismic velocities for zero-age oceanic crust at fast-spreading MOR dominated by hydrothermal circulation processes. First, we examine a number of velocity-permeability relationships available in the literature to obtain plausible fine-scale 2-D permeability models for upper oceanic crust along ~20-km-long portion of the EPR 9°50′ N. Second, to provide valid constraints to our preferred permeability model, we compare our results extracted at L-vent with collocated permeability estimates from poroelastic response to tidal loading. At this location, our preferred permeability model suggests average permeabilities $10^{-12.75}$ and $10^{-14.05}$ m^2 for layers 2A and 2B, respectively. When the preferred permeability-velocity relationships are extended in 2-D, for layer 2A permeabilities vary ~$10^{-12.7}$–$10^{-10.3}$ m^2, with an average value $10^{-11.2}$ m^2. For layer 2B the range of permeabilities within the 2-D model is broader, spanning the values ~10^{-17}–10^{-10} m^2, with an average 10^{-14} m^2. Finally, to test our results, we use numerical modeling to examine the development of hydrothermal circulation flow patterns within a constant permeability field and the ones developed employing our preferred fine-scale permeability model. Our results clearly show that the assumption of uniform permeability field leads to regularly spaced upflows that develop along the entire model, which is not supported by seafloor observations. In contrast, by employing our preferred permeability model, we are able to depict the presence and distribution of the upflow conduits that are comparable to the location of discharge zones observed in the seafloor, including the two vent fields.

Previous studies emphasized that relating velocities and crustal permeabilities is not a straight forward problem (e.g., Wilcock & Fisher, 2004) and often highly spatially heterogeneous (e.g., Arnoux et al., 2017; Arnulf et al., 2011). However, to advance our knowledge behind hydrothermal processes, we need to aim at building more realistic hydrothermal numerical models, which among others requires quantitative permeability estimates in space and time from various independent approaches that can be compared and then contrasted with the observables.

Acknowledgments
We thank P. Audhkhasi for his help with the effective medium theory code. We also thank W. S. D. Wilcock for early discussions (during a visit at IPGP as an invited professor in 2016) on using *Vp*-derived permeability field in hydrothermal flow modeling. We are grateful to T. Henstock and anonymous reviewer whose suggestions and comments significantly improved the manuscript. All MCS field data collected along the ridge axis are archived at the Academic Seismic Portal (doi:10.7284/901987). The velocity model used in this study is archived under the Academic Seismic Portal at UTIG (doi:10.1594/IEDA/500019). Files with the temperature fields resulting from our numerical modeling are archived under Open Science Framework (doi:10.17605/OSF.IO/3ST2N). Numerical computations were performed on the S-CAPAD platform, IPGP, Paris, France. This work was partly supported by the CNRS INSU-SYSTER program.

References

Arnoux, G. M., Toomey, D. R., Hooft, E. E. E., Wilcock, W. S. D., Morgan, J., Warner, M., & VanderBeek, B. P. (2017). Seismic evidence that black smoker heat flux is influenced by localized magma replenishment and associated increases in crustal permeability. *Geophysical Research Letters*, *44*, 1687–1695. https://doi.org/10.1002/2016GL071990

Arnulf, A. F., Harding, A. J., Kent, G. M., & Wilcock, W. S. D. (2018). Structure, seismicity, and accretionary processes at the hot spot-influenced Axial Seamount on the Juan de Fuca Ridge. *Journal of Geophysical Research: Solid Earth*, *123*, 4618–4646. https://doi.org/10.1029/2017JB015131

Arnulf, A. F., Harding, A. J., Singh, S. C., Kent, G. M., & Crawford, W. (2012). Fine-scale velocity structure of upper oceanic crust from full waveform inversion of downward continued seismic reflection data at the Lucky Strike volcano, mid-Atlantic ridge. *Geophysical Research Letters*, *39*, L08303. https://doi.org/10.1029/2012GL051064

Arnulf, A. F., Harding, A. J., Singh, S. C., Kent, G. M., & Crawford, W. (2014). Nature of upper crust beneath the Lucky Strike volcano using elastic full waveform inversion of streamer data. *Geophysical Journal International*, *196*(3), 1471–1491. https://doi.org/10.1093/gji/ggt461

Arnulf, A. F., Singh, S. C., Harding, A. J., Kent, G. M., & Crawford, W. (2011). Strong seismic heterogeneity in layer 2A near hydrothermal vents at the mid-Atlantic ridge. *Geophysical Research Letters*, *38*, L13320. https://doi.org/10.1029/2011GL047753

Baker, E. T. (2009). Relationships between hydrothermal activity and axial magma chamber distribution, depth, and melt content. *Geochemistry, Geophysics, Geosystems*, *10*, Q06009. https://doi.org/10.1029/2009GC002424

Baker, E. T., Resing, J. A., Haymon, R. M., Tunnicliffe, V., Lavelle, J. W., Martinez, F., et al. (2016). How many vent fields? New estimates of vent field populations on ocean ridges from precise mapping of hydrothermal discharge locations. *Earth and Planetary Science Letters*, *449*, 186–196. https://doi.org/10.1016/j.epsl.2016.05.031

Barreyre, T., Escartin, J., Sohn, R., & Cannat, M. (2014). Permeability of the Lucky Strike deep-sea hydrothermal system: Constraints from the poroelastic response to ocean tidal loading. *Earth and Planetary Science Letters*, *408*, 146–154. https://doi.org/10.1016/j.epsl.2014.09.049

Barreyre, T., Olive, J.-A., Crone, T. J., & Sohn, R. A. (2018). Depth-dependent permeability and heat output at basalt-hosted hydrothermal systems across mid-ocean ridge spreading rates. *Geochemistry, Geophysics, Geosystems*, *19*, 1259–1281. https://doi.org/10.1002/2017GC007152

Barreyre, T., & Sohn, R. A. (2016). Poroelastic response of mid-ocean ridge hydrothermal systems to ocean tidal loading: Implications for shallow permeability structure. *Geophysical Research Letters*, *43*, 1660–1668. https://doi.org/10.1002/2015GL066479

Beaulieu, S. E., Baker, E. T., & German, C. R. (2015). Where are the undiscovered vents on oceanic spreading ridges? *Deep Sea Research*, *121*, 202–212. https://doi.org/10.1016/j.dsr2.2015.05.001

Beaulieu, S. E., Baker, E. T., German, C. R., & Maffei, A. (2013). An authoritative global database for active submarine hydrothermal vent fields. *Geochemistry, Geophysics, Geosystems*, *14*, 4892–4905. https://doi.org/10.1002/2013GC004998

Becker, K. (1989). Drilling deep into young oceanic crust, Hole 504B, Costa Rica rift. *Reviews of Geophysics*, *27*(1), 79–102.

Becker, K., & Davis, E. (2003). New evidence for age variation and scale effects of permeabilities of young oceanic crust from borehole thermal and pressure measurements. *Earth and Planetary Science Letters*, *210*, 499–508.

Becker, K., & Fisher, A. T. (2000). Permeability of upper oceanic basement on the eastern flank of the Juan de Fuca Ridge determined with drill-string packer experiments. *Journal of Geophysical Research*, *105*, 879–912.

Becker, K., & Fisher, A. T. (2008). Borehole packer tests at multiple depths resolve distinct hydrologic intervals in 3.5-Ma upper oceanic crust on the eastern flank of Juan de Fuca Ridge. *Journal of Geophysical Research*, *113*, B07105. https://doi.org/10.1029/2007JB005446

Canales, J. P., Singh, S. C., Detrick, R. S., Carbotte, S. M., Harding, A. J., Kent, G. M., et al. (2006). Seismic evidence for variations in axial magma chamber properties along the southern Juan de Fuca Ridge. *Earth and Planetary Science Letters*, *246*(3-4), 353–366. https://doi.org/10.1016/j.epsl.2006.04.032

Carbotte, S. M., Marjanović, M., Carton, H. D., Mutter, J. C., Canales, J. P., Nedimović, M. R., et al. (2013). Fine-scale segmentation of the crustal magma reservoir beneath the East Pacific Rise. *Nature Geoscience*, *6*(10), 866–870. https://doi.org/10.1038/ngeo1933

Carlson, R. L. (2010). How crack porosity and shape control seismic velocities in the upper oceanic crust: Modeling downhole logs from Holes 504B and 1256D. *Geochemistry, Geophysics, Geosystems*, *11*, Q04007. https://doi.org/10.1029/2009GC002955

Carlson, R. L. (2011). The effect of hydrothermal alteration on the seismic structure of the upper oceanic crust: Evidence from Holes 504B and 1256D. *Geochemistry, Geophysics, Geosystems*, *12*, Q09013. https://doi.org/10.1029/2011GC003624

Carlson, R. L. (2014). The influence of porosity and crack morphology on seismic velocity and permeability in the upper oceanic crust. *Geochemistry, Geophysics, Geosystems*, *15*, 10–27. https://doi.org/10.1002/2013GC004965

Christeson, G. L., Morgan, J. V., & Warner, M. R. (2012). Shallow oceanic crust: Full waveform tomographic images of the seismic layer 2A/2B boundary. *Journal of Geophysical Research*, *117*, B05101. https://doi.org/10.1029/2011JB008972

Coumou, D., Driesner, T., & Heinrich, C. A. (2008). The structure and dynamics of mid-ocean ridge hydrothermal systems. *Science*, *321*(5897), 1825–1828. https://doi.org/10.1126/science.1159582

Coumou, D., Geiger, S., Driesner, T., Heinrich, C. A., & Matthai, S. K. (2006). The dynamics of mid-ocean ridge hydrothermal systems: Splitting plumes and fluctuating vent temperatures. *Earth and Planetary Science Letters*, *245*(1-2), 218–231. https://doi.org/10.1016/j.epsl.2006.02.044

Crone, T. J., Tolstoy, M., & Stroup, D. F. (2011). Permeability structure of young ocean crust from poroelastically triggered earthquakes. *Geophysical Research Letters*, *38*, L05305. https://doi.org/10.1029/2011GL046820

Davis, E., LaBonte, A., He, J., Becker, K., & Fisher, A. (2010). Thermally stimulated29This article is protected by copyright. All rights reserved."runaway" downhole flow in a superhydrostatic ocean crustal borehole:Observations, simulations, and inferences regarding crustal permeability. *Journal of Geophysical Research*, *115*, B07102. https://doi.org/10.1029/2009JB006986

Detrick, R. S., Buhl, P., Vera, E., Mutter, J., Orcutt, J., Madsen, J., & Brocher, T. (1987). Multi-channel seismic imaging of a crustal magma chamber along the East Pacific Rise. *Nature*, *326*(6108), 35–41. https://doi.org/10.1038/326035a0

Driesner, T. (2010). The interplay of permeability and fluid properties as a first order control of heat transport, venting temperatures and venting salinities at mid-ocean ridge hydrothermal systems. *Geofluids*, *10*(1–2), 132–141.

Elderfield, H., & Schultz, A. (1996). Mid-ocean ridge hydrothermal fluxes and the chemical composition of the ocean. *Annual Review of Earth and Planetary Sciences*, *24*(1), 191–224. https://doi.org/10.1146/annurev.earth.24.1.191

Fisher, A. T. (1998). Permeability within basaltic oceanic crust. *Reviews of Geophysics*, *36*(2), 143–182.

Fisher, A. T., Davis, E. E., & Becker, K. (2008). Borehole-to-borehole hydrologic response across 2.4 km in the upper oceanic crust: Implications for crustal-scale properties. *Journal of Geophysical Research*, *113*, B07106. https://doi.org/10.1029/2007JB005447

Fontaine, F. J., & Wilcock, W. S. D. (2007). Two-dimensional numerical models of open-top hydrothermal convection at high Rayleigh and Nusselt numbers: Implications for mid-ocean ridge hydrothermal circulation. *Geochemistry, Geophysics, Geosystems*, *8*, Q07010. https://doi.org/10.1029/2007GC001601

Gillis, K. M. (2002). The rootzone of an ancient hydrothermal system exposed in the Troodos ophiolite, Cyprus. *The Journal of Geology*, *110*(1),57–74. https://doi.org/10.1086/324205

Gillis, K. M. (2008). The roof of an axial magma chamber: A hornfelsic heat exchanger. *Geology*, *36*(4), 299–302. https://doi.org/10.1130/G24590A.1

Gillis, K. M., & Roberts, M. D. (1999). Cracking at the magma-hydrothermal transition: Evidence from the Troodos ophiolite, Cyprus. *Earth andPlanetary Science Letters*, *169*(3–4), 227–244. https://doi.org/10.1016/S0012-821X(99)00087-4

Hasenclever, J., Theissen-Krah, S., Rüpke, L. H., Morgan, J. P., Iyer, K., Petersen, S., & Devey, C. W. (2014). Hybrid shallow on-axis and deepoff-axis hydrothermal circulation at fast-spreading ridges. *Nature*, *508*(7497), 508–512. https://doi.org/10.1038/nature13174

Haymon, R. M., Fornari, D. J., Edwards, M. H., Carbotte, S., Wright, D., & Macdonald, K. C. (1991). Hydrothermal vent distribution along the East Pacific Rise crest (9°090-9°540N) and its relationship to magmatic and tectonic processes on fast spreading mid-ocean ridges. *Earth and Planetary Science Letters*, *104*(2-4), 513–534. https://doi.org/10.1016/0012-821X(91)90226-8

Henstock, T. J., Woods, A. W., & White, R. S. (1993). The accretion of oceanic crust by episodic sill intrusion. *Journal of Geophysical Research*, *98*(B3), 4143–4161. https://doi.org/10.1029/92JB02661

Kent, G. M., Harding, A. J., & Orcutt, J. A. (1993). Distribution of magma beneath the East Pacific Rise between the Clipperton transform and the 9°170N Deval from forward modeling of common depth point data. *Journal of Geophysical Research*, *98*(B8), 13945–13969. https://doi.org/10.1029/93JB00705

Lowell, R. P., Farough, A., Hoover, J., & Cummings, K. (2013). Characteristics of magma-driven hydrothermal systems at oceanic spreading centers. *Geochemistry, Geophysics, Geosystems*, *14*, 1756–1770. https://doi.org/10.1002/ggge.20109

Lowell, R. P., & Germanovich, L. N. (1994). On the temporal evolution of high-temperature hydrothermal systems at ocean ridge crests. *Journal of Geophysical Research*, *99*(B1), 565–575. https://doi.org/10.1029/93JB02568

Lowell, R. P., & Germanovich, L. N. (2004). Hydrothermal processes at mid-ocean ridges: Results from scale analysis and single-pass models. In C. R. German (Ed.), *Mid-ocean ridges: Hydrothermal interactions between the lithosphere and oceans*, *Geophysical Monograph Series*, (Vol. 148, pp. 219–244). Washington, DC: American Geophysical Union.

Marjanović, M., Carbotte, S. M., Carton, H., Nedimović, M. R., Canales, J. P., & Mutter, J. C. (2018). Crustal magmatic system beneath the East Pacific Rise (8°20′ to 10°10′ N): Implications for tectono-magmatic segmentation and melt transport at fast-spreading ridges. *Geochemistry, Geophysics, Geosystems*, *19*, 4584–4611. https://doi.org/10.1029/2018GC007590

Marjanović, M., Carton, H. D., Nedimović, M. R., Carbotte, S. M., Mutter, J. C., & Canales, J. P. (2015). Distribution of melt along the East Pacific Rise from 9°300 to 10°N from an amplitude variation with angle of incidence (AVA) technique. *Geophysical Journal International*, *203*(1), 1–21. https://doi.org/10.1093/gji/ggv251

Marjanović, M., Fuji, N., Singh, S. C., Belahi, T., & Escartín, J. (2017). Seismic signatures of hydrothermal pathways along the East Pacific Rise between 9°16′ and 9°56′N. *Journal of Geophysical Research: Solid Earth*, *122*, 10,241–10,262. https://doi.org/10.1002/2017JB015004

Marjanović, M., Plessix, R.-É., Stopin, A., & Singh, S. C. (2018). Elastic versus acoustic 3-D full waveform inversion at the East Pacific Rise 9°50′N. *Geophysical Journal International*, ggy503. https://doi.org/10.1093/gji/ggy503

Marjanović M., A. Stopin, R.E. Plessix & S.C. Singh (2017). Three-dimensional mapping of extrusive layer at the East Pacific Rise 9°50′N, *AGU Fall Meeting in New Orleans*, Abstract V44A-01.

Mavko, G., & Nur, A. (1997). The effect of a percolation threshold in the Kozeny-Carman relation. *Geophysics*, *62*(5), 1480-1482.

MacLeod, C. J., & Yaouancq, G. (2000). A fossil melt lens in the Oman ophiolite: Implications for magma chamber processes at fast spreadingridges. *Earth and Planetary Science Letters*, *176*(3–4), 357–373. https://doi.org/10.1016/S0012-821X(00)00020-0

Morgan, J. P., & Chen, Y. J. (1993). The genesis of oceanic crust: Magma injection, hydrothermal circulation, and crustal flow. *Journal of Geophysical Research*, *98*(B4), 6283–6297. https://doi.org/10.1029/92JB02650

Morgan, J., Warner, M., Arnoux, G., Hooft, E., Toomey, D., VanderBeek, B., & Wilcock, W. (2016). Nextgeneration seismic experiments-II: Wideangle,multi-azimuth, 3-D, full-waveform inversion of sparse field data. *Geophysical Journal International*, *204*(2), 1342–1363. https://doi.org/10.1093/gji/ggv513

Mutter, J. C., Carbotte, S. M., Nedimović, M. R., Canales, J. P., & Carton, H. D. (2009). Seismic imaging in three dimensions on the East Pacific Rise. *Eos, Transactions of the American Geophysical Union*, *90*(42), 374–375. https://doi.org/10.1029/2009EO420002

Nehlig, P. (1994). Fracture and permeability analysis in magma-hydrothermal transition zones in the Samail ophiolite (Oman). *Journal of Geophysical Research*, *99*(B1), 589–601. https://doi.org/10.1029/93JB02569

Nicolas, A., & Boudier, F. (2011). Structure and dynamics of ridge axial melt lenses in the Oman ophiolite. *Journal of Geophysical Research*, *116*, B03103. https://doi.org/10.1029/2010JB007934

Pedersen, R. B. (1986). The nature and significance of magma chamber margins in ophiolites: Examples from the Norwegian Caledonides. *Earth and Planetary Science Letters*, *77*(1), 100–112. https://doi.org/10.1016/0012-821X(86)90136-6

Sclater, J. G., Jaupart, C., & Galson, D. (1980). The heat flow through oceanic and continental crust and the heat loss of the earth. *Reviews of Geophysics and Space Physics*, *18*(1), 269–311. https://doi.org/10.1029/RG018i001p00269

Singh, S. C., Collier, J. S., Harding, A. J., Kent, G. M., & Orcutt, J. A. (1999). Seismic evidence for a hydrothermal layer above the solid roof of the axialmagma chamber at the southern East Pacific Rise. *Geology*, *27*(3), 219–222. https://doi.org/10.1130/0091-7613(1999)027<0219:SEFAHL>2.3.CO;2

Singh, S. C., Kent, G. M., Collier, J. S., Harding, A. J., & Orcutt, J. A. (1998). Melt to mush variations in crustal magma properties along the ridge crest at the southern East Pacific Rise. *Nature*, *394*(6696), 874–878. https://doi.org/10.1038/29740

Slagle, A. L., & Goldberg, D. S. (2011). Evaluation of ocean crustal Sites 1256 and 504 for long-term CO2 sequestration. *Geophysical Research Letters*, *38*, L16307. https://doi.org/10.1029/2011GL048613

Sohn, R. A., Webb, S. C., & Hildebrand, J. A. (2004). Fine-scale seismic structure of the shallow volcanic crust on the East Pacific Rise at 9°50′N. *Journal of Geophysical Research*, *109*, B12104. https://doi.org/10.1029/2004JB003152

Soule, S. A., Escartín, J., & Fornari, D. J. (2009). A record of eruption and intrusion at a fast spreading ridge axis: Axial summit trough of the East Pacific Rise at 9–10N. *Geochemistry, Geophysics, Geosystems*, *10*, Q10T07. https://doi.org/10.1029/2008GC002354

Stein, C. A., & Stein, S. (1992). A model for the global variation in oceanic depth and heat flow with lithospheric age. *Nature*, *359*(6391), 123–129. https://doi.org/10.1038/359123a0

Swift, S., Reichow, M., Tikku, A., Tominaga, M., & Gilbert, L. (2008). Velocity structure of upper ocean crust at Ocean Drilling Program Site 1256. *Geochemistry, Geophysics, Geosystems*, *9*, Q10O13. https://doi.org/10.1029/2008GC002188

Tan, Y. J., Tolstoy, M., Waldhauser, F., & Wilcock, W. S. (2016). Dynamics of a seafloor-spreading episode at the East Pacific Rise. *Nature*, *540*(7632), 261–265. https://doi.org/10.1038/nature20116

Theissen-Krah, S., Iyer, K., Rüpke, L. H., & Morgan, J. P. (2011). Coupled mechanical and hydrothermal modeling of crustal accretion at intermediate to fast spreading ridges. *Earth and Planetary Science Letters*, *311*(3), 275–286.

Tolstoy, M., Cowen, J. P., Baker, E. T., Fornari, D. J., Rubin, K. H., Shank, T. M., et al. (2006). A sea-floor spreading event captured by seismometers. *Science*, *314*(5807), 1920–1922. https://doi.org/10.1126/science.1133950

Tolstoy, M., Waldhauser, F., Bohnenstiehl, D. R., Weekly, R. T., & Kim, W.-Y. (2008). Seismic identification of along-axis hydrothermal flow on the East Pacific Rise. *Nature*, *415*, 181–184.

Vera, E. E., Mutter, J. C., Buhl, P., Orcutt, J. A., Harding, A. J., Kappus, M. E., et al. (1990). The structure of 0- to 0.2-m.y.-old oceanic crust at 9°N on the East Pacific Rise from expanded spread profiles. *Journal of Geophysical Research*, *95*(B10), 15,529–15,556. https://doi.org/10.1029/JB095iB10p15529

Waldhauser, F., & Tolstoy, M. (2011). Seismogenic structure and processes associated with magma inflation and hydrothermal circulation beneath the East Pacific Rise at 9°500N. *Geochemistry, Geophysics, Geosystems*, *12*, Q08T10. https://doi.org/10.1029/2011GC003568

White, S. M., Haymon, R. M., & Carbotte, S. (2006). A new view of ridge segmentation and near-axis volcanism at the East Pacific Rise, 8-12°N, from EM300 multibeam bathymetry. *Geochemistry, Geophysics, Geosystems*, *7*, Q12O05. https://doi.org/10.1029/2006GC001407

Wilcock, W. S. D., & Fisher, A. T. (2004). Geophysical constraints on the sub-seafloor environment near mid-ocean ridges. In W. S. D. Wilcock (Ed.), *The subseafloor biosphere at mid-ocean ridges*, *Geophysical Monograph Series* (Vol. 144, pp. 51–74). Washington, DC: American Geophysical Union. https://doi.org/10.1029/144GM05

Wilcock, W. S. D., & McNabb, A. (1996). Estimates of crustal permeability on the Endeavour segment of the Juan de Fuca mid-ocean ridge. *Earth and Planetary Science Letters*, *138*(1–4), 83–91. https://doi.org/10.1016/0012-821X(95)00225-2

Winslow, D. M., Fisher, A. T., & Becker, K. (2013). Characterizing borehole fluid flow and formation permeability in the ocean crust using linked analytic models and Markov chain Monte Carlo analysis. *Geochemistry, Geophysics, Geosystems*, *14*, 3857–3874. https://doi.org/10.1002/ggge.20241

Xu, M., Canales, J. P., Carbotte, S. M., Carton, H., Nedimović, M. R., & Mutter, J. C. (2014). Variations in axial magma lens properties along the East Pacific Rise (9°30′-10°00′N) from swath 3D seismic imaging and 1D waveform inversion. *Journal of Geophysical Research: Solid Earth*, *119*, 2721–2744. https://doi.org/10.1002/2013JB010730

References From the Supporting Information

Budiansky, B. (1965). On the elastic moduli of some heterogeneous materials. *Journal of the Mechanics and Physics of Solids*, *13*(4), 223–227. https://doi.org/10.1016/0022-5096(65)90011-6

Carlson, R. L., & Raskin, G. S. (1984). density of ocean crust. *Nature*, *311*(5986), 555–558. https://doi.org/10.1038/311555a0

Cleary, M. P., Chen, I.-W., & Lee, S.-M. (1980). Self-consistent techniques for heterogeneous media. *American Society of Civil Engineers Journal of Engineering Mechanics*, *106*, 861–887.

Hill, R. (1965). A self-consistent mechanics of composite materials. *Journal of the Mechanics and Physics of Solids*, *13*(4), 213–222. https://doi.org/10.1016/0022-5096(65)90010-4

McLaughlin, R. A. (1977). A study of the differential scheme for composite materials. *International Journal of Engineering Science*, *15*(4), 237–244. https://doi.org/10.1016/0020-7225(77)90058-1

Nedimović, M. R., Carbotte, S. M., Diebold, J. B., Harding, A. J., Canales, J. P., & Kent, G. M. (2008). Upper crustal evolution along the Juan de Fuca ridge flanks. *Geochemistry, Geophysics, Geosystems*, *9*, Q09006. https://doi.org/10.1029/2008GC002085

Newman, K. R., Nedimović, M. R., Canales, J. P., & Carbotte, S. M. (2011). Evolution of seismic layer 2B across the Juan de Fuca Ridge from hydrophone streamer 2-D traveltime tomography. *Geochemistry, Geophysics, Geosystems*, *12*, Q05009. https://doi.org/10.1029/2010GC003462

Norris, A. N. (1985). A differential scheme for the effective moduli of composites. *Mechanics of Materials*, *4*(1), 1–16. https://doi.org/10.1016/0167-6636(85)90002-X

Taylor, M. A. J., & Singh, S. C. (2002). Composition and microstructure of magma bodies from effective medium theory. *Geophysical Journal International*, *149*(1), 15–21. https://doi.org/10.1046/j.1365-246X.2002.01577.x

Warner, M. R., Morgan, J. V., Umpleby, A., Štekl, I. & Guasch, L., (2012). Which physics for full wavefield inversion?, in 74th EAGE Conference and Exhibition incorporating EUROPEC 2012, EAGE, Extended Abstracts, pp. 2994–2998.

Wu, T. T. (1966). The effect of inclusion shape on the elastic moduli of a two-phase material. *International Journal of Solids and Structures*, *2*(1), 1–8. https://doi.org/10.1016/0020-7683(66)90002-3